

THE NUMERICAL STUDY ON INFLUENCE  
OF THE OPEN SQUARE CAVITY WITH INTERNAL HEAT SOURCE

A. SHAREEF<sup>\*a</sup>, R. SIVA PRASAD<sup>b</sup>

<sup>a</sup>Research Scholar, Department of Mathematics,  
Rayalaseema University, Kurnool, Andhra Pradesh 518007, India.

<sup>b</sup>Department of Mathematics,  
Sri Krishnadevaraya University, Anantapuram, Andhra Pradesh 515003, India.

(Received On: 11-01-18; Revised & Accepted On: 08-02-18)

---

ABSTRACT

In the current study, Finite Element Method has been used to convert the non-linear coupled partial differential equations for flow and temperature field into a matrix form of equations, which can be solved iteratively with the help of a computer code. The Galerkin Finite Element Method of three noded triangular elements is used to divide the physical domain into smaller segments, which is a pre-requisite for finite element method. Numerical results are presented in terms of stream functions, isotherms, temperature profiles and Nusselt numbers.

**Keywords:** Viscous fluid, Heat transfer, Fluid Mechanics, Finite element methods.

**Subject Classification Codes 2010:** 76DXX, 35Q79, 35Q35, 74S05.

---

1. INTRODUCTION

In recent decades, research on natural convection in cavities has been the subject of many studies. Natural convection in open cavities and slots is encountered in many engineering applications, such as solar thermal receivers, heat convection from extended surfaces in heat exchangers, and solar energy collectors with insulated strips [1]. Cavities with a side opening and internal heat source can be seen in many electronic devices, where the openings facilitate the cooling of the internal components of the apparatus. Furthermore, the study of this case is relevant in many other applications, among which can be cited: construction and operation of nuclear reactors, solar energy collectors, energy storage systems, design and construction of indoor environments, and grain storage. Many studies have been reported in the literature, where the behavior of fluids within the cavities was evaluated, some of which are cited below. The natural convection in cavities induced by the difference in temperature between vertical (or horizontal) walls is a case widely studied [2–15]. In those studies, the authors evaluated the influence of the temperature difference [2–5, 7–12], aspect ratio, opening and inclinations of the cavity [6, 13, 15] on the fluid thermal behavior inside it. A numerical study on heat distribution and thermal mixing during steady laminar natural convective flow within fluid-saturated porous square cavities has been considered for three different cases: uniformly heated bottom wall, discrete heat sources on walls, and uniformly heated left and bottom walls in Kaluri *et al.* [10]. Deng and Chang [11] study numerically a two dimensional steady and laminar natural convection in an air-filled rectangular enclosure where the horizontal walls are thermally insulated and the vertical side walls have two spatially varying sinusoidal temperature distributions of different amplitudes and phases. Michalek [12] conducted experiments to measure the water flow inside a cubical cavity with isothermal vertical walls and adiabatic horizontal walls for values of Ra greater than  $10^9$ .

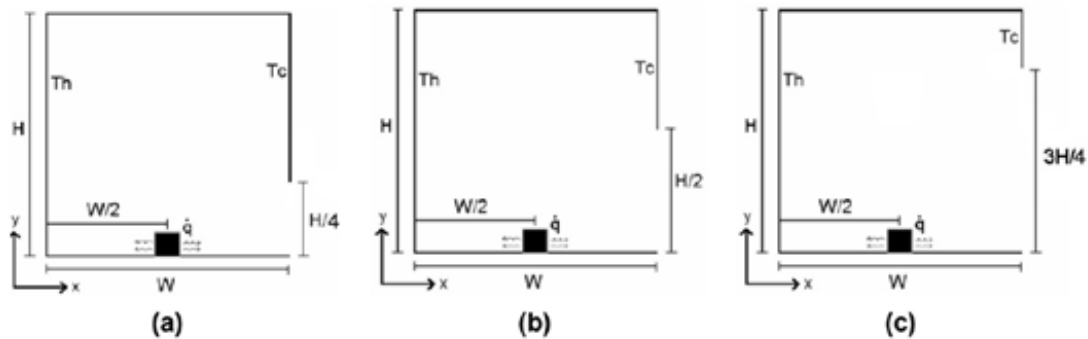
The transition from stationary to non-stationary flow was below the theoretical value of the critical Rayleigh number. Bilgen and Oztop [13] performed a numerical study of heat transfer by natural convection in an inclined and partially open 2D cavity. A parametric study was conducted for values of Ra between 103 and 106, concluding that the value of Nusselt number was maximized for angles between 30° and 60° for low values of Ra, while at high values of Ra, the value of the Nusselt number was maximized for angles between 60 and 90. Kuznik *et al.* [14] used the Lattice–Boltzmann method with a non-uniform mesh for the simulation of natural convection in a square cavity.

---

Corresponding Author: A. Shareef<sup>\*a</sup>,

<sup>a</sup>Research Scholar, Department of Mathematics,  
Rayalaseema University, Kurnool, Andhra Pradesh 518007, India.

The authors determined the Rayleigh numbers for the transition region between  $10^3$  and  $10^9$ , and observed a good agreement with those reported in the literature. The same method was used by Mezrhab *et al.* [15], where the influence of the cavity inclination and the existence of an internal partition were evaluated. There was a maximum reduction in heat transfer for the range of Rayleigh numbers between  $6 \times 10^3$  and  $2 \times 10^4$ . Some study combine effect of radiation and natural convection in cavities differentially heated [16– 18]. When there is an internal heat source in cavities large changes in the internal flow characteristics occur. Studies on natural convection in cavities with internal heat source can be found in Kuznetsov and Sheremet [19], Nakhi and Chamkha [20], Oztop and Bilgen [21], Oztop and Abu-Nada [22], and Bazylak *et al.* [23], or with internal baffles in Fontana *et al.* [24]. In many cases, the cavity presents a partial opening, which facilitates mass flow and therefore the cooling process [25–29]. Mariani and Silva [28] conducted a numerical study of the thermal and fluid dynamics behavior of air in partially open 2D enclosures based on two aspects of the radius,  $H/W = 1$  and 2. The enclosure had an opening on the right wall and a small heat source located on the bottom or left wall, occupying three different positions. Numerical simulations were performed for Ra in the range of  $10^3$  and  $10^6$  and it was found that changes in this parameter have significant effects on the average and local Nusselt numbers (Nu) of the enclosures. Another study was conducted by Mariani and Coelho [29] to investigate steady heat transfer and flow phenomena of natural convection of air in enclosures, with three aspect ratios ( $H/W = 1, 2,$  and  $4$ ), within which there is a local heat source on the bottom wall at three different positions. A similar study was carried out by Kandaswamy *et al.* [30], where the influence of the position and the size of the heat source were evaluated. This study was conducted for Grashof numbers between  $10^3$  and  $10^5$ . Hence, this study investigates natural convection in a partially open square cavity with an opening in the right wall of three different sizes  $H/4, H/2,$  and  $3H/4$ , where  $H$  is the cavity height. The cavity was submitted to temperature differences between the left and right vertical walls and had an internal heat conduction source. The influence of the internal heat source at intensities of  $R = 400, 1000$  and  $2000$ , and external Rayleigh numbers of  $10^3 \leq Ra \leq 10^5$ , on the thermal and fluid dynamics of the air inside the cavity and the mass inflow rate at the opening, was investigated.



## 2. MATHEMATICAL FORMULATION

Fig. 1 shows a schematic diagram of the problem under consideration and the coordinate system. The system to be considered is a two-dimensional square cavity of width  $W$  and height  $H$ , where the two vertical walls are kept at different temperatures,  $T_h$  (left wall) and  $T_c$  (right wall),  $T_h > T_c$ . Zero heat flow is assumed at the top and bottom walls. The walls are rigid and no-slip conditions are imposed at the boundaries. The internal heat source is placed on the bottom horizontal wall, midway between the vertical walls, occupying 1% of the total volume of the cavity. The opening is placed on the right vertical wall of the cavity being evaluated for three conditions  $H/ = H/4, H/2,$  and  $3H/4$ . The flow field is considered to be steady and the fluid is incompressible. Thermo physical properties of the fluid are assumed constant, with the exception of the density variation in the buoyancy term, i.e., the Boussinesq approximation is valid. The equations for the conservation of momentum and energy are

$$\frac{\partial u}{\partial x} + \frac{\partial v}{\partial y} = 0 \quad (3.1)$$

$$u \frac{\partial v}{\partial x} + v \frac{\partial v}{\partial y} = -\frac{1}{\rho} \frac{\partial p}{\partial y} + \mathcal{G} \left( \frac{\partial^2 v}{\partial x^2} + \frac{\partial^2 v}{\partial y^2} \right) + g\beta(T - T_c) \quad (3.2)$$

$$u \frac{\partial T}{\partial x} + v \frac{\partial T}{\partial y} = \alpha \left( \frac{\partial^2 T}{\partial x^2} + \frac{\partial^2 T}{\partial y^2} \right) \quad (3.3)$$

with boundary conditions

$$\begin{aligned} u(x, 0) = u(x, H) = u(0, y) = u(H, y) = 0, \\ v(x, 0) = v(x, H) = v(0, y) = v(H, y) = 0, \\ T(x, 0) = T_h, \end{aligned}$$

$$\frac{\partial T}{\partial y}(x, H) = 0, \quad T(0, y) = T_h - (T_h - T_c) \frac{y}{H},$$

$$T(H, y) = T_h - (T_h - T_c) \frac{y}{H}, \quad \frac{\partial T}{\partial y}(x, H) = 0, \quad 0 < x < H$$

The Continuity equation (3.1) can be satisfied automatically by introducing the stream function ‘ $\psi$ ’ as

$$u = \frac{\partial \psi}{\partial y} \tag{3.4a}$$

$$v = -\frac{\partial \psi}{\partial x} \tag{3.4b}$$

where  $x$  and  $y$  are the distances measured along the horizontal and vertical directions respectively  $u$  and  $v$  are the velocity components in the  $x$  and  $y$  directions respectively  $T$  denotes the temperature  $\nu$  and  $\alpha$  are kinematic viscosity and thermal diffusivity respectively  $K$  is the medium permeability  $P$  is the pressure and  $\rho$  is the density  $T_h$  and  $T_c$  are the temperatures at hot bottom wall and cold vertical wall respectively  $L$  is the side of the square cavity.

Using the following non dimensional variables,

Width  $X = \frac{x}{H}$

Height  $Y = \frac{y}{H}$

Velocity components  $\begin{cases} U = \frac{uH}{\alpha} \\ V = \frac{vH}{\alpha} \end{cases}$

Stream function  $\bar{\psi} = \frac{\psi}{\alpha}$

Pressure  $P = \frac{pH^2}{\rho\alpha^2}$

Prandtl Number  $Pr = \frac{\nu}{\alpha}$

Rayleigh number  $Ra = \frac{g\beta(T_h - T_c)H^3 Pr}{\nu^2}$

Temperature  $\theta = \frac{T - T_c}{T_h - T_c}$

The governing equations (3.1)-(3.3) reduce to non-dimensional form as

$$\frac{\partial U}{\partial X} + \frac{\partial V}{\partial Y} = 0 \tag{3.5}$$

$$U \frac{\partial V}{\partial X} + V \frac{\partial V}{\partial Y} = -\frac{\partial P}{\partial Y} + Pr \left( \frac{\partial^2 V}{\partial X^2} + \frac{\partial^2 V}{\partial Y^2} \right) + Ra Pr \theta \tag{3.6}$$

$$U \frac{\partial \theta}{\partial X} + V \frac{\partial \theta}{\partial Y} = \left( \frac{\partial^2 \theta}{\partial X^2} + \frac{\partial^2 \theta}{\partial Y^2} \right) \tag{3.7}$$

with the non dimensional boundary conditions are

$$U(X, 0) = U(X, 1) = U(0, Y) = U(1, Y) = 0,$$

$$V(X, 0) = V(X, 1) = V(0, Y) = V(1, Y) = 0,$$

$$\theta(X, 0) = 1, \quad \frac{\partial \theta}{\partial Y}(X, 1) = 0, \quad \theta(0, Y) = \theta(1, Y) = 1 - Y$$

where  $X$  and  $Y$  are dimensionless coordinates varying along horizontal and vertical directions respectively  $U$  and  $V$  are dimensionless velocity components in the  $X$  and  $Y$  directions respectively  $\theta$  is the dimensionless temperature  $P$  is the dimensionless pressure  $Ra$  and  $Pr$  are Rayleigh Prandtl numbers respectively.

### 3. SOLUTION OF PROBLEM

Thus far we have derived the partial differential equations, which describe the heat and fluid flow behavior in the vicinity of porous medium. The development of governing equations is one part but the second and important part is to solve these equations in order to predict the various parameters of interest in the porous medium. There are various numerical methods available to achieve the solution of these equations, but the most popular numerical methods are Finite difference method, Finite volume method and the Finite element method. The selection of these numerical methods is an important decision, which is influenced by variety of factors amongst which the geometry of domain plays a vital role. Other factors include the ease with which these partial differential equations can be transformed into simple forms, the computational time required and the flexibility in development of computer code to solve these equations. In the present study, we have predominantly used Finite Element Method (FEM). The following sections enlighten the Finite element method and present its application to solve the above-mentioned equations.

The Finite Element Method is a deservingly popular method amongst scientific community. This method was originally developed to study the mechanical stresses in a complex airframe structure popularized by Zienkiewicz and Cheung (23) by applying it to continuum mechanics. Since then the application of Finite Element Method has been exploited to solve the numerous problems in various engineering disciplines. The great thing about finite element method is its ease with which it can be generalized to myriad engineering problems comprised of different materials. Another admirable feature of the Finite Element Method (FEM) is that it can be applied wide range of geometries having irregular boundaries, which is highly difficult to achieve with other contemporary methods. FEM can be said to have comprised of roughly 5 steps to solve any particular problem. The steps can be summarized as

- **Discretizing the domain:** This step involves the division of whole physical domain into smaller segments known as elements, and then identifying the nodes, coordinates of each node and ensuring proper connectivity between the nodes.
- **Specifying the equation:** In this step, the governing equation is specified and an equation is written in terms of nodal values
- **Development of Global matrix:** The equations are arranged in a global matrix which takes into account the whole domain
- **Solution:** The equations are solved to get the desired variable at each table in the domain
- **Evaluate the quantities of interest:** After solving the equations a set of values is obtained for each node, which can be further processed to get the quantities of interest.

There are varieties of elements available in FEM, which are distinguished by the presence of number of nodes. The present study is carried out by using a simple 3-noded triangular element as shown in fig. 2

Let us consider that the variable to be determined in the triangular area is ' $\theta$ '. The polynomial function for ' $\theta$ ' can be expressed as:

$$\theta = \alpha_1 + \alpha_2 x + \alpha_3 y \tag{1}$$

The variable  $\theta$  has the value  $\theta_i$ ,  $\theta_j$  and  $\theta_k$  at the nodal position i, j, and k of the element. The x and y coordinates at these points are  $x_i$ ,  $x_j$ ,  $x_k$  and  $y_i$ ,  $y_j$  and  $y_k$  respectively. Substitution of these nodal values in the equation (1) helps in determining the constants  $\alpha_1$ ,  $\alpha_2$ ,  $\alpha_3$  which are:

$$\alpha_1 = \frac{1}{2A} [(x_j y_k - x_k y_j) \theta_i + (x_k y_i - x_i y_k) \theta_j + (x_i y_j - x_j y_i) \theta_k] \tag{2}$$

$$\alpha_2 = \frac{1}{2A} [(y_j - y_k) \theta_i + (y_k - y_i) \theta_j + (y_i - y_j) \theta_k] \tag{3}$$

$$\alpha_3 = \frac{1}{2A} [(x_k - x_j) \theta_i + (x_i - x_k) \theta_j + (x_j - x_i) \theta_k] \tag{4}$$

where A is area of the triangle given as

$$2A = \begin{vmatrix} 1 & x_i & y_i \\ 1 & x_j & y_j \\ 1 & x_k & y_k \end{vmatrix} \tag{5}$$

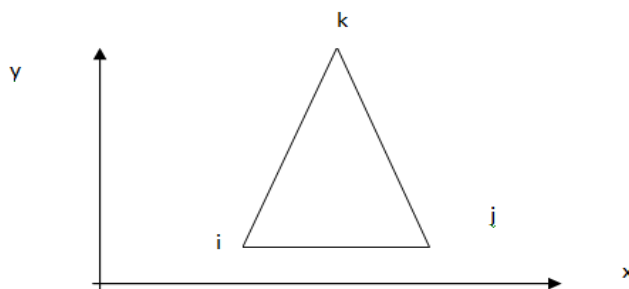


**Figure-2:** Typical triangular element

Substitution of  $\alpha_1, \alpha_2, \alpha_3$  in the equation (1) and mathematical arrangement of the terms results into

$$\theta = N_i \theta_i + N_j \theta_j + N_k \theta_k \quad (6)$$

In equation (6),  $N_i, N_j$  and  $N_k$  are the shape function given by

$$N_m = \frac{a_m + b_m x + c_m y}{2A}, \quad m = i, j, k \quad (7)$$

The constants can be expressed in terms of coordinates as

$$a_i = x_j y_k - x_k y_j \quad (8a)$$

$$b_i = y_j - y_k$$

$$c_i = x_k - x_j$$

$$a_j = x_k y_i - x_i y_k$$

$$b_j = y_k - y_i$$

$$c_j = x_i - x_k$$

$$a_k = x_i y_j - x_j y_i$$

$$b_k = y_i - y_j$$

$$c_k = x_j - x_i$$

The triangular element can be subdivided into three triangles with a point in the center of original triangle as shown in fig.3.

Defining the new area ratios as

$$L_1 = \frac{\text{area } pij}{\text{area } ijk} \quad (9a)$$

$$L_2 = \frac{\text{area } pj k}{\text{area } ijk} \quad (9b)$$

$$L_3 = \frac{\text{area } pki}{\text{area } ijk} \quad (9c)$$

It can be shown that

$$L_1 = N_1 \quad (10a)$$

$$L_2 = N_2 \quad (10b)$$

$$L_3 = N_3 \quad (10c)$$

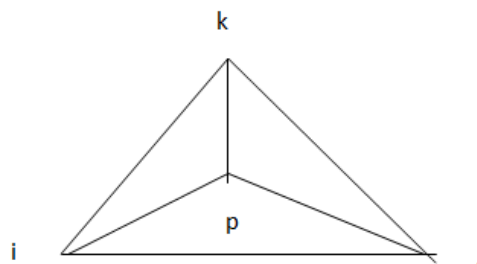


**Figure-3:** showing the sub triangular areas

Good insight into the FEM is given in Segerlind [24], Galerkin method is employed to convert the partial differential equations into matrix form for an element. The steps invented are as given below. Please note that the nodal terms  $i, j$  &  $k$  are replaced by 1,2 & 3 respectively in subsequent discussions for simplicity.

The momentum and energy balance equations are solved using the Galerkin finite element method. Continuity equation will be used as a constraint due to mass conservation and this constraint may be used to obtain the pressure distribution. In order to solve equations, we use the finite element method where the pressure  $P$  is eliminated by a penalty parameter  $\gamma$  and the incompressibility criteria given by equation (3.5) which results in

$$P = -\gamma \left( \frac{\partial U}{\partial X} + \frac{\partial V}{\partial Y} \right) \quad (3.8)$$

The continuity equation (3.5) is automatically satisfied for large values of  $\gamma$ .

Using equation (3.8) and introducing stream function, the momentum equation (3.6) reduce to

$$U \frac{\partial V}{\partial X} + V \frac{\partial V}{\partial Y} = \gamma \frac{\partial}{\partial Y} \left( \frac{\partial U}{\partial X} + \frac{\partial V}{\partial Y} \right) + \text{Pr} \left( \frac{\partial^2 V}{\partial X^2} + \frac{\partial^2 V}{\partial Y^2} \right) + Ra \text{Pr} \theta \quad (3.9)$$

Finally momentum equation put in the form

$$\left[ \frac{\partial \bar{\psi}}{\partial Y} \frac{\partial^2 \bar{\psi}}{\partial X \partial Y} - \frac{\partial \bar{\psi}}{\partial X} \frac{\partial^2 \bar{\psi}}{\partial Y^2} \right] = \gamma \left( \frac{\partial^2 \bar{\psi}}{\partial Y^2} \frac{\partial \bar{\psi}}{\partial X} + \frac{\partial^2 \bar{\psi}}{\partial Y^2} \right) + \text{Pr} \left[ \frac{\partial^2 \bar{\psi}}{\partial X^2} + \frac{\partial^2 \bar{\psi}}{\partial Y^2} \right] - Ra \text{Pr} \theta \quad (3.10)$$

Application of Galerkin method to equation (3.10) yields:

$$\{R^e\} = - \int_A N^T \left\{ \begin{array}{l} \left[ \frac{\partial \bar{\psi}}{\partial Y} \frac{\partial^2 \bar{\psi}}{\partial X \partial Y} - \frac{\partial \bar{\psi}}{\partial X} \frac{\partial^2 \bar{\psi}}{\partial Y^2} \right] - \gamma \left( \frac{\partial^2 \bar{\psi}}{\partial Y^2} \frac{\partial \bar{\psi}}{\partial X} + \frac{\partial^2 \bar{\psi}}{\partial Y^2} \right) \\ - \text{Pr} \left[ \frac{\partial^2 \bar{\psi}}{\partial X^2} + \frac{\partial^2 \bar{\psi}}{\partial Y^2} \right] + Ra \text{Pr} \theta \end{array} \right\} dXdY \quad (3.11)$$

where  $R^e$  is the residue.

Considering the terms individually

$$\int_A [N]^T \frac{\partial \bar{\psi}}{\partial Y} \frac{\partial^2 \bar{\psi}}{\partial X \partial Y} dA = \frac{1}{4A} \begin{Bmatrix} c_1 \bar{\psi}_1 + c_2 \bar{\psi}_2 + c_3 \bar{\psi}_3 \\ c_1 \bar{\psi}_1 + c_2 \bar{\psi}_2 + c_3 \bar{\psi}_3 \\ c_1 \bar{\psi}_1 + c_2 \bar{\psi}_2 + c_3 \bar{\psi}_3 \end{Bmatrix} [b_1, b_2, b_3] \quad (3.12)$$

$$\int_A [N^T] \frac{\partial \bar{\psi}}{\partial X} \frac{\partial^2 \bar{\psi}}{\partial Y^2} dA = \frac{1}{12A} \begin{Bmatrix} b_1 \bar{\psi}_1 + b_2 \bar{\psi}_2 + b_3 \bar{\psi}_3 \\ b_1 \bar{\psi}_1 + b_2 \bar{\psi}_2 + b_3 \bar{\psi}_3 \\ b_1 \bar{\psi}_1 + b_2 \bar{\psi}_2 + b_3 \bar{\psi}_3 \end{Bmatrix} [c_1, c_2, c_3] \quad (3.13)$$

$$\int_A [N^T] \gamma \frac{\partial^2 \bar{\psi}}{\partial Y^2} \frac{\partial \bar{\psi}}{\partial X} dA = \frac{\gamma}{12A} \begin{Bmatrix} b_1 \bar{\psi}_1 + b_2 \bar{\psi}_2 + b_3 \bar{\psi}_3 \\ b_1 \bar{\psi}_1 + b_2 \bar{\psi}_2 + b_3 \bar{\psi}_3 \\ b_1 \bar{\psi}_1 + b_2 \bar{\psi}_2 + b_3 \bar{\psi}_3 \end{Bmatrix} [c_1, c_2, c_3] \quad (3.14)$$

$$\int_A [N^T] \gamma \frac{\partial^2 \bar{\psi}}{\partial Y^2} dA = -\frac{\gamma}{4A} \begin{bmatrix} b_1^2 & b_1 b_2 & b_1 b_3 \\ b_1 b_2 & b_2^2 & b_2 b_3 \\ b_1 b_3 & b_2 b_3 & b_3^2 \end{bmatrix} \begin{bmatrix} \theta_1 \\ \theta_2 \\ \theta_3 \end{bmatrix} \quad (3.15)$$

$$\int_A [N^T] \text{Pr} \frac{\partial^2 \bar{\psi}}{\partial X^2} dA = -\frac{\text{Pr}}{4A} \begin{bmatrix} c_1^2 & c_1 c_2 & c_1 c_3 \\ c_1 c_2 & c_2^2 & c_2 c_3 \\ c_1 c_3 & c_2 c_3 & c_3^2 \end{bmatrix} \begin{bmatrix} \theta_1 \\ \theta_2 \\ \theta_3 \end{bmatrix}$$

$$\int_A [N^T] \text{Pr} \frac{\partial^2 \bar{\psi}}{\partial Y^2} dA = -\frac{\text{Pr}}{4A} \begin{bmatrix} b_1^2 & b_1 b_2 & b_1 b_3 \\ b_1 b_2 & b_2^2 & b_2 b_3 \\ b_1 b_3 & b_2 b_3 & b_3^2 \end{bmatrix} \begin{bmatrix} \theta_1 \\ \theta_2 \\ \theta_3 \end{bmatrix} \quad (3.16)$$

$$\int_A [N]^T RaP \theta dA = \frac{RaP}{12A} \begin{bmatrix} \theta_1 \\ \theta_2 \\ \theta_3 \end{bmatrix} \quad (3.17)$$

Thus the whole equation (3.10) can be written in matrix form as

$$\begin{aligned} & \frac{1}{4A} \begin{Bmatrix} c_1\bar{\psi}_1 + c_2\bar{\psi}_2 + c_3\bar{\psi}_3 \\ c_1\bar{\psi}_1 + c_2\bar{\psi}_2 + c_3\bar{\psi}_3 \\ c_1\bar{\psi}_1 + c_2\bar{\psi}_2 + c_3\bar{\psi}_3 \end{Bmatrix} [b_1, b_2, b_3] - \frac{1}{12A} \begin{Bmatrix} b_1\bar{\psi}_1 + b_2\bar{\psi}_2 + b_3\bar{\psi}_3 \\ b_1\bar{\psi}_1 + b_2\bar{\psi}_2 + b_3\bar{\psi}_3 \\ b_1\bar{\psi}_1 + b_2\bar{\psi}_2 + b_3\bar{\psi}_3 \end{Bmatrix} [c_1, c_2, c_3] \\ & + \frac{\gamma}{12A} \begin{Bmatrix} b_1\bar{\psi}_1 + b_2\bar{\psi}_2 + b_3\bar{\psi}_3 \\ b_1\bar{\psi}_1 + b_2\bar{\psi}_2 + b_3\bar{\psi}_3 \\ b_1\bar{\psi}_1 + b_2\bar{\psi}_2 + b_3\bar{\psi}_3 \end{Bmatrix} [c_1, c_2, c_3] + \frac{\gamma}{4A} \begin{bmatrix} b_1^2 & b_1b_2 & b_1b_3 \\ b_1b_2 & b_2^2 & b_2b_3 \\ b_1b_3 & b_2b_3 & b_3^2 \end{bmatrix} \begin{bmatrix} \theta_1 \\ \theta_2 \\ \theta_3 \end{bmatrix} \\ & - \frac{\text{Pr}}{4A} \begin{bmatrix} c_1^2 & c_1c_2 & c_1c_3 \\ c_1c_2 & c_2^2 & c_2c_3 \\ c_1c_3 & c_2c_3 & c_3^2 \end{bmatrix} \begin{bmatrix} \theta_1 \\ \theta_2 \\ \theta_3 \end{bmatrix} + \frac{\text{Pr}}{4A} \begin{bmatrix} b_1^2 & b_1b_2 & b_1b_3 \\ b_1b_2 & b_2^2 & b_2b_3 \\ b_1b_3 & b_2b_3 & b_3^2 \end{bmatrix} \begin{bmatrix} \theta_1 \\ \theta_2 \\ \theta_3 \end{bmatrix} + \frac{\text{RaP}}{12A} \begin{bmatrix} \theta_1 \\ \theta_2 \\ \theta_3 \end{bmatrix} = 0 \end{aligned} \quad (3.18)$$

Introducing stream function, the energy equation (3.7) reduces as

$$\frac{\partial \bar{\psi}}{\partial Y} \frac{\partial \theta}{\partial X} + \frac{\partial \bar{\psi}}{\partial X} \frac{\partial \theta}{\partial Y} = \left( \frac{\partial^2 \theta}{\partial X^2} + \frac{\partial^2 \theta}{\partial Y^2} \right) \quad (3.19)$$

FEM of Energy Equation is

$$\{R^e\} = - \int_A [N]^T \left( \frac{\partial \bar{\psi}}{\partial Y} \frac{\partial \theta}{\partial X} + \frac{\partial \bar{\psi}}{\partial X} \frac{\partial \theta}{\partial Y} - \frac{\partial^2 \theta}{\partial X^2} - \frac{\partial^2 \theta}{\partial Y^2} \right) dA \quad (3.20)$$

Considering the terms individually

$$\int_A [N]^T \frac{\partial \bar{\psi}}{\partial Y} \frac{\partial \theta}{\partial X} dA = \frac{1}{12A} \begin{Bmatrix} c_1\bar{\psi}_1 + c_2\bar{\psi}_2 + c_3\bar{\psi}_3 \\ c_1\bar{\psi}_1 + c_2\bar{\psi}_2 + c_3\bar{\psi}_3 \\ c_1\bar{\psi}_1 + c_2\bar{\psi}_2 + c_3\bar{\psi}_3 \end{Bmatrix} [b_1, b_2, b_3] \begin{bmatrix} \theta_1 \\ \theta_2 \\ \theta_3 \end{bmatrix} \quad (3.21)$$

$$\int_A [N]^T \frac{\partial \bar{\psi}}{\partial X} \frac{\partial \theta}{\partial Y} dA = \frac{1}{12A} \begin{Bmatrix} b_1\bar{\psi}_1 + b_2\bar{\psi}_2 + b_3\bar{\psi}_3 \\ b_1\bar{\psi}_1 + b_2\bar{\psi}_2 + b_3\bar{\psi}_3 \\ b_1\bar{\psi}_1 + b_2\bar{\psi}_2 + b_3\bar{\psi}_3 \end{Bmatrix} [c_1, c_2, c_3] \begin{bmatrix} \theta_1 \\ \theta_2 \\ \theta_3 \end{bmatrix} \quad (3.22)$$

$$\int_A [N]^T \frac{\partial^2 \theta}{\partial X^2} dA = - \frac{1}{4A} \begin{bmatrix} b_1^2 & b_1b_2 & b_1b_3 \\ b_1b_2 & b_2^2 & b_2b_3 \\ b_1b_3 & b_2b_3 & b_3^2 \end{bmatrix} \begin{bmatrix} \theta_1 \\ \theta_2 \\ \theta_3 \end{bmatrix} \quad (3.23)$$

$$\int_A [N]^T \frac{\partial^2 \theta}{\partial Y^2} dA = - \frac{1}{4A} \begin{bmatrix} c_1^2 & c_1c_2 & c_1c_3 \\ c_1c_2 & c_2^2 & c_2c_3 \\ c_1c_3 & c_2c_3 & c_3^2 \end{bmatrix} \begin{bmatrix} \theta_1 \\ \theta_2 \\ \theta_3 \end{bmatrix} \quad (3.24)$$

Thus the whole equation (3.19) can be written in matrix form as

$$\begin{aligned} & \frac{1}{12A} \begin{Bmatrix} c_1\bar{\psi}_1 + c_2\bar{\psi}_2 + c_3\bar{\psi}_3 \\ c_1\bar{\psi}_1 + c_2\bar{\psi}_2 + c_3\bar{\psi}_3 \\ c_1\bar{\psi}_1 + c_2\bar{\psi}_2 + c_3\bar{\psi}_3 \end{Bmatrix} [b_1, b_2, b_3] \begin{bmatrix} \theta_1 \\ \theta_2 \\ \theta_3 \end{bmatrix} - \frac{1}{12A} \begin{Bmatrix} b_1\bar{\psi}_1 + b_2\bar{\psi}_2 + b_3\bar{\psi}_3 \\ b_1\bar{\psi}_1 + b_2\bar{\psi}_2 + b_3\bar{\psi}_3 \\ b_1\bar{\psi}_1 + b_2\bar{\psi}_2 + b_3\bar{\psi}_3 \end{Bmatrix} [c_1, c_2, c_3] \begin{bmatrix} \theta_1 \\ \theta_2 \\ \theta_3 \end{bmatrix} \\ & - \frac{1}{4A} \begin{bmatrix} b_1^2 & b_1b_2 & b_1b_3 \\ b_1b_2 & b_2^2 & b_2b_3 \\ b_1b_3 & b_2b_3 & b_3^2 \end{bmatrix} \begin{bmatrix} \theta_1 \\ \theta_2 \\ \theta_3 \end{bmatrix} + \frac{1}{4A} \begin{bmatrix} c_1^2 & c_1c_2 & c_1c_3 \\ c_1c_2 & c_2^2 & c_2c_3 \\ c_1c_3 & c_2c_3 & c_3^2 \end{bmatrix} \begin{bmatrix} \theta_1 \\ \theta_2 \\ \theta_3 \end{bmatrix} = 0 \end{aligned} \quad (3.25)$$

#### 4. NUSSLET NUMBER

The average dimensionless Nusselt Number ( $\overline{Nu}$ ) can be evaluated using the formula

$$\overline{Nu} = -\frac{\partial \theta}{\partial n} \tag{3.26}$$

where n denotes the normal direction on a plane.

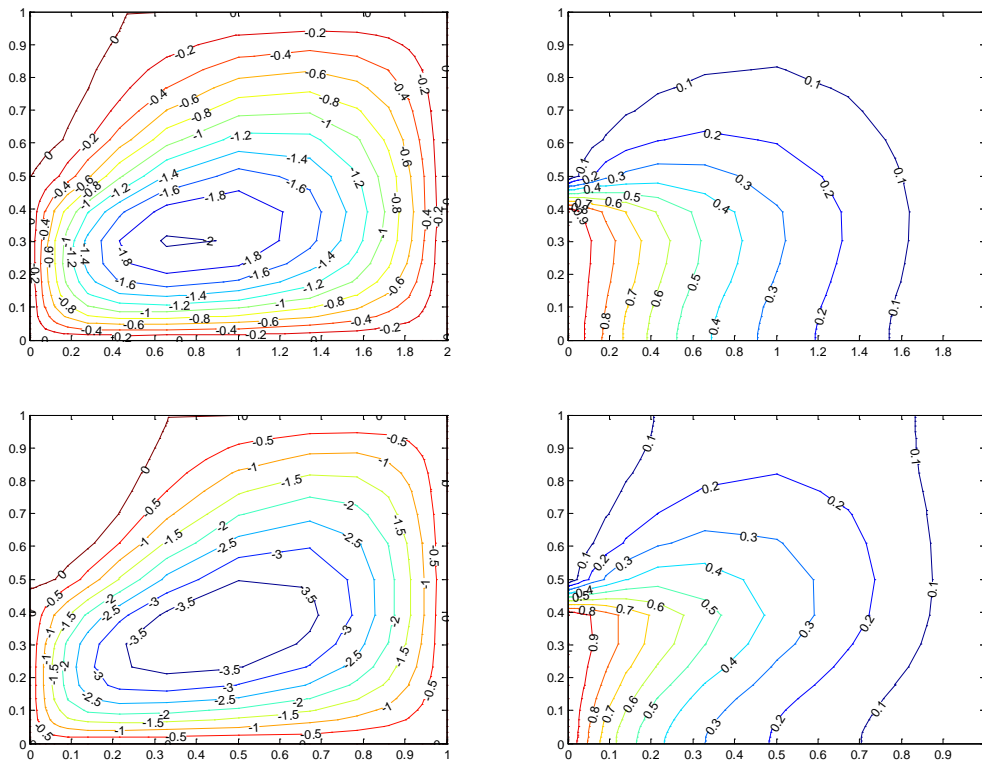
The average Nusselt numbers at bottom wall ( $\overline{Nu}_b$ ) and at the side wall ( $\overline{Nu}_s$ ) are defined as

$$\overline{Nu}_b = \int_0^1 Nu_b dX \tag{3.27}$$

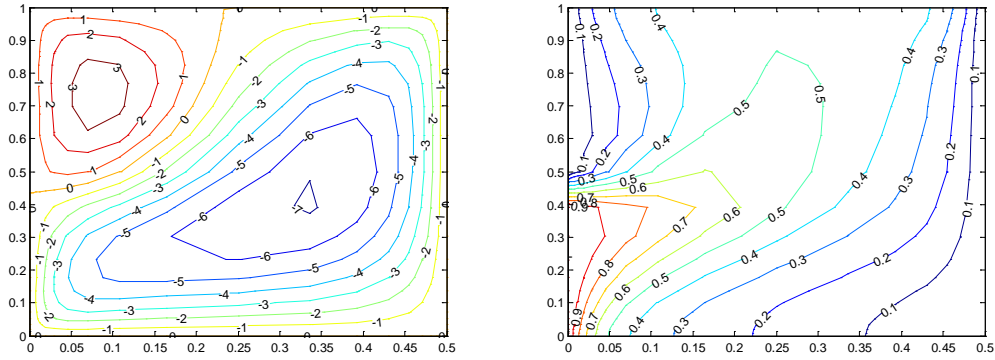
$$\overline{Nu}_s = \int_0^1 Nu_s dY \tag{3.28}$$

#### 5. RESULTS AND DISCUSSION

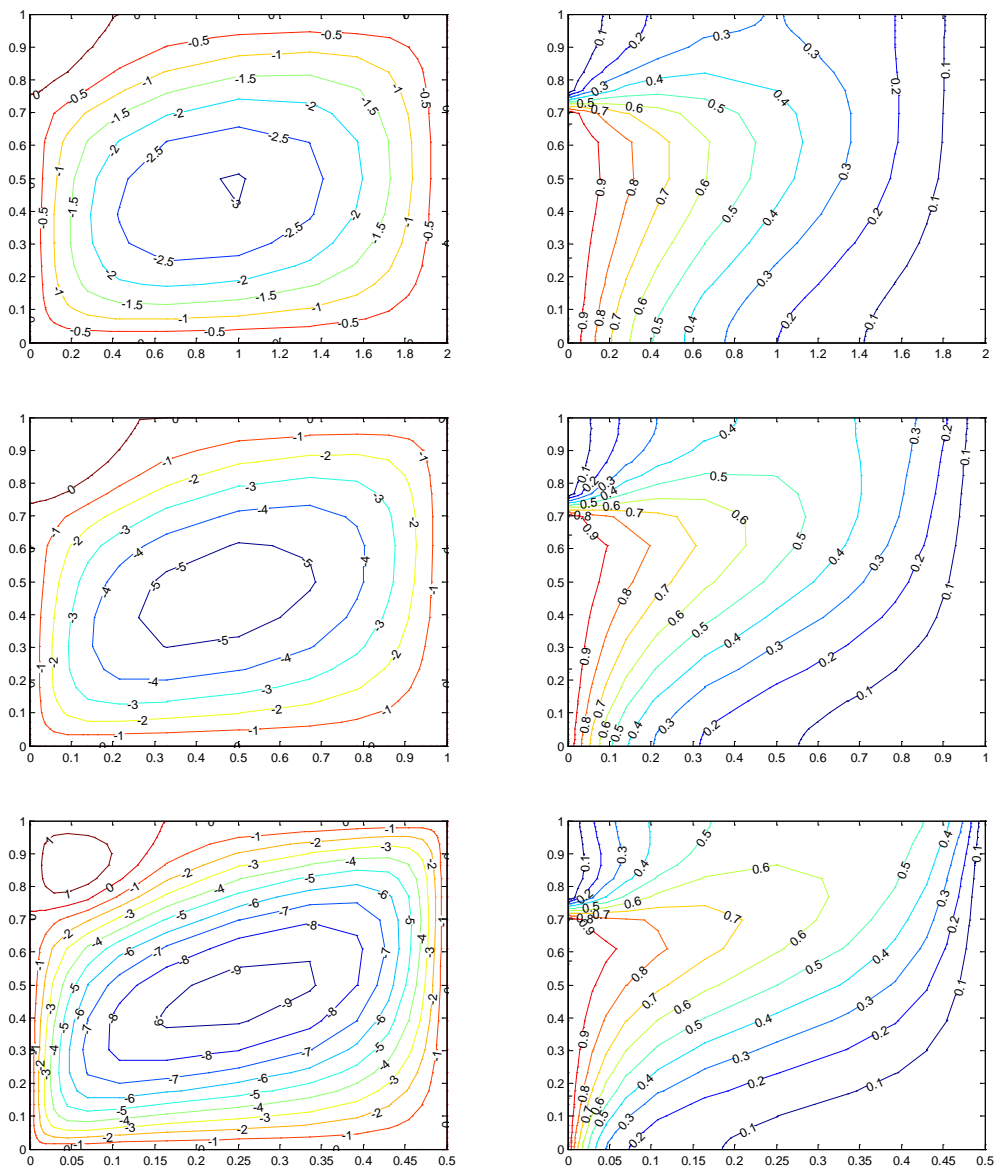
The computational domain consists of  $20 \times 20$  bi-quadratic elements which correspond to  $41 \times 41$  grid points. The bi-quadratic elements with lesser number of nodes smoothly capture the non-linear variations of the field variables which are in contrast with finite element method solutions available. Figs. 4 – 9 illustrate the stream function and isotherm contours for various values of  $Ra = 10^3-10^5$  and  $Pr = 0.7-10$  with uniformly heated bottom wall and linearly heated side walls where the top wall is well insulated. As expected due to the linearly heated vertical walls and the uniformly heated bottom wall, fluids rise up from the middle portion of the bottom wall and flow down along two vertical walls forming two symmetric rolls with clockwise and anti-clockwise rotations inside the cavity. At  $Ra = 10^3$ , the magnitudes of stream functions are considerably lower and the heat transfer is due to purely conduction. During conduction dominant heat transfer the temperature  $\theta \leq 0.3$  occur symmetrically near the side walls of the enclosure. The other temperature contours with  $\theta \geq 0.4$  are smooth curves which span the entire enclosure and they are generally symmetric with respect to the vertical symmetric line. The temperature contours as indicated in Fig. 4 remains invariant up to  $Ra < 10^4$ . At  $Ra = 10^4$ , the circulation near the central regimes are stronger and consequently, the temperature contour with  $\theta = 0.5$  starts getting shifted towards



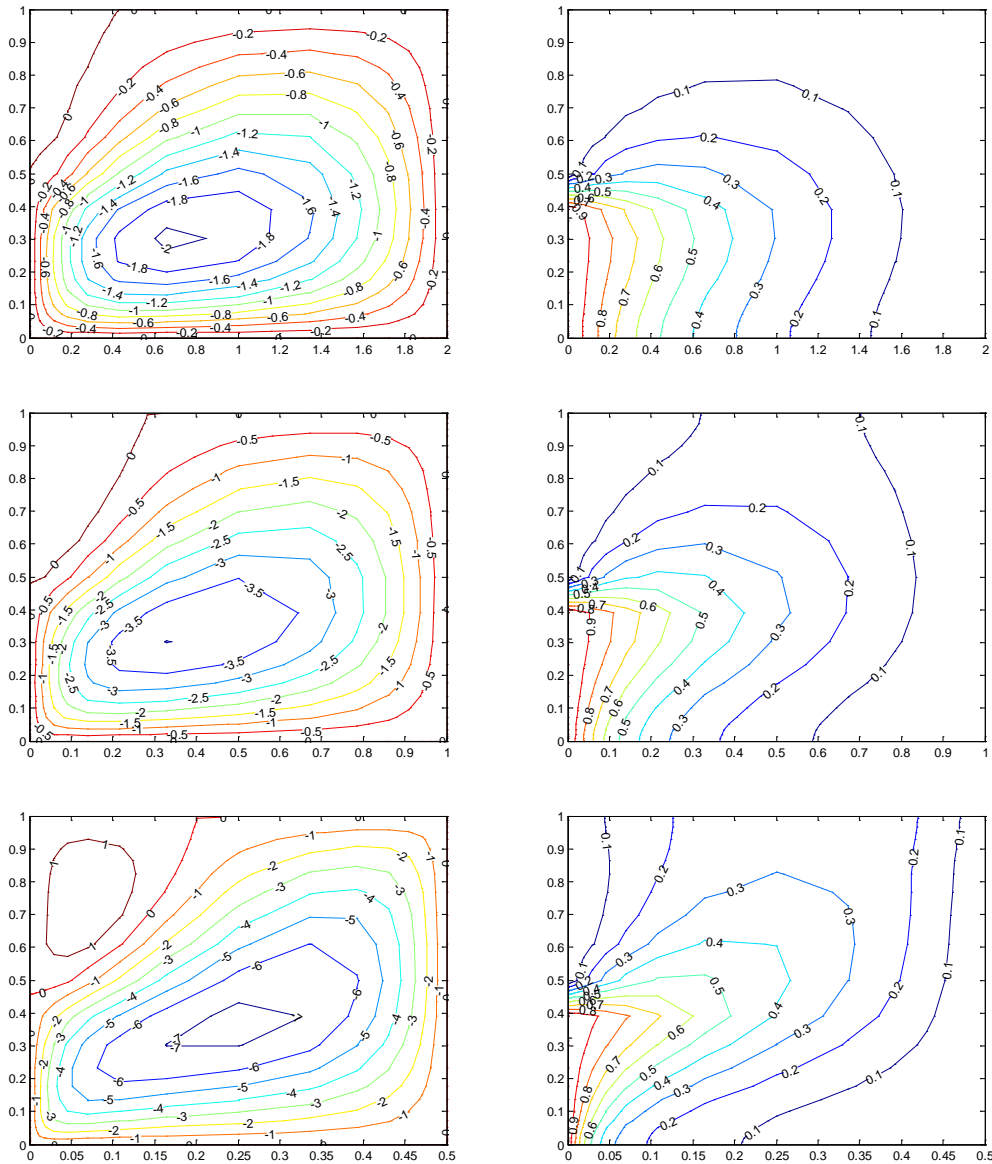




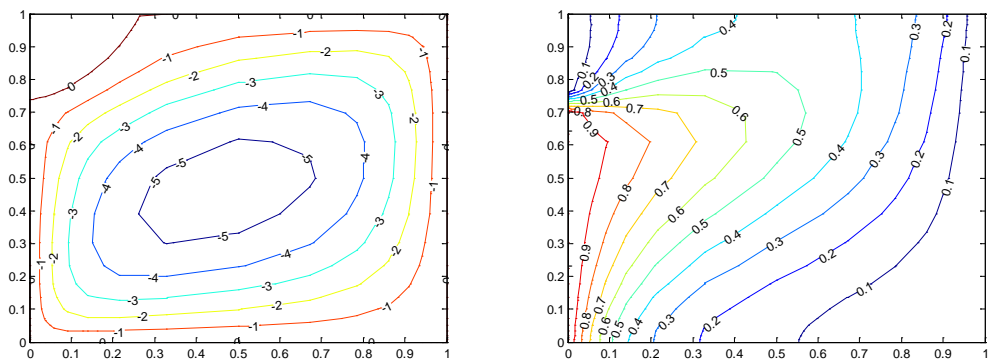
**Figure-4:** Contour plots for linearly heated vertical walls,  $\theta(0, Y) = \theta(1, Y) = 1 - Y$  with  $Pr = 0.7$  and  $Ra = 10^3$ . Clockwise and anti-clockwise flows are shown via negative and positive signs of stream functions (Left) and Isotherms (Right) respectively.

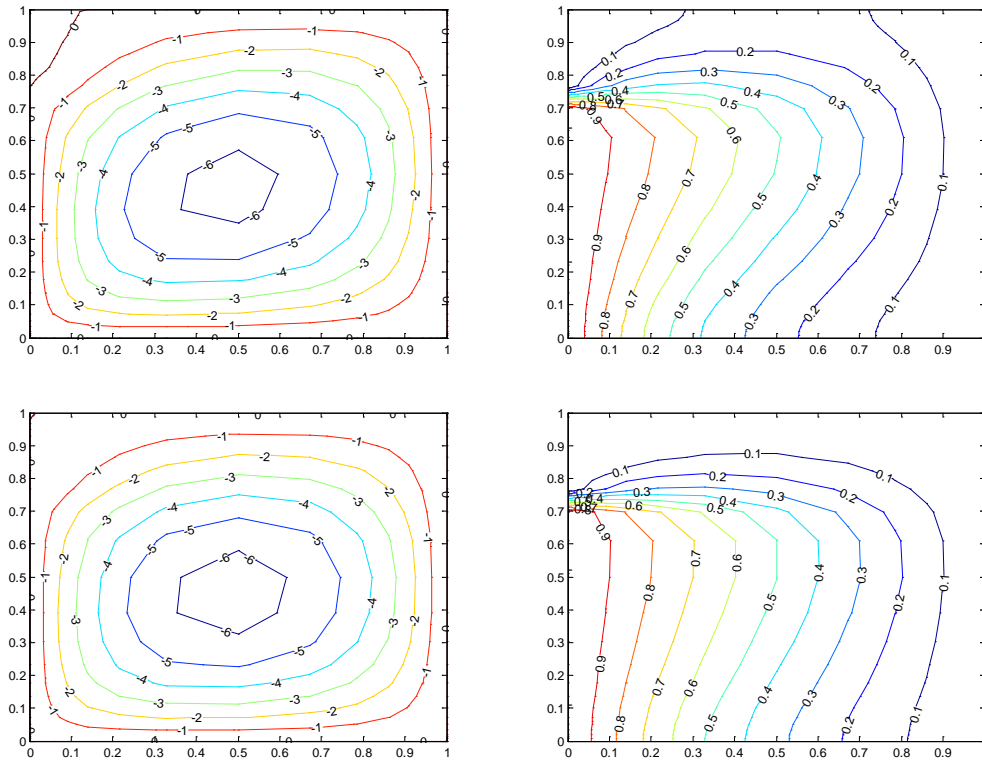


**Figure-5:** Contour plots for linearly heated vertical walls,  $\theta(0, Y) = \theta(1, Y) = 1 - Y$  with  $Pr = 0.7$  and  $Ra = 10^4$ . Clockwise and anti-clockwise flows are shown via negative and positive signs of stream functions (Left) and Isotherms (Right) respectively.

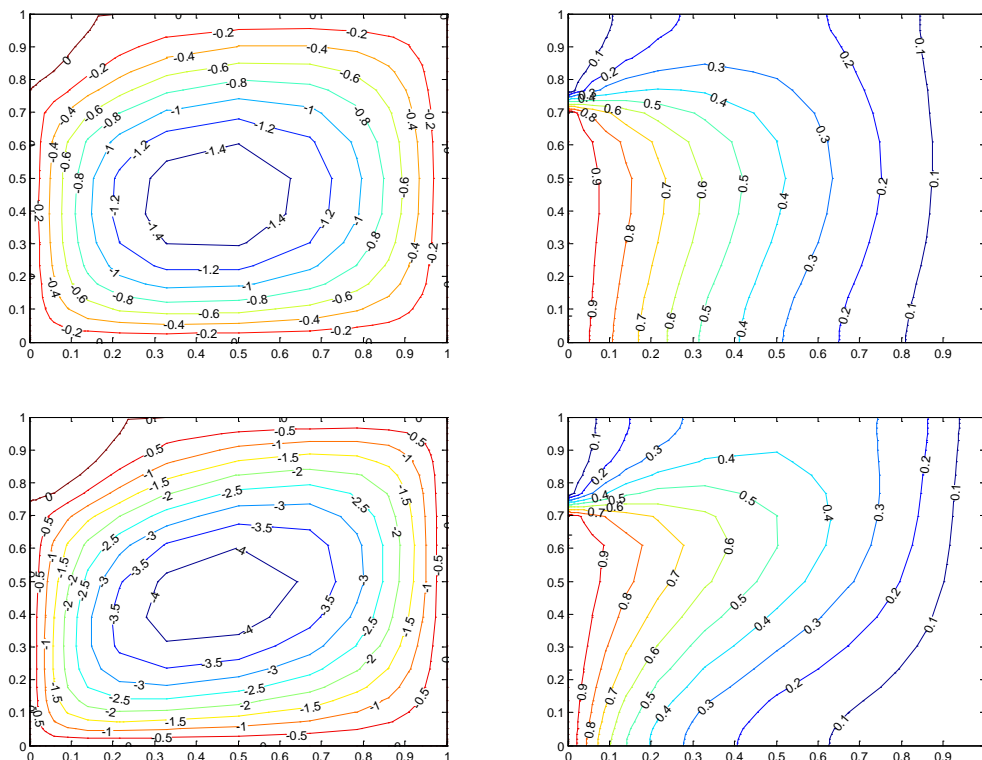


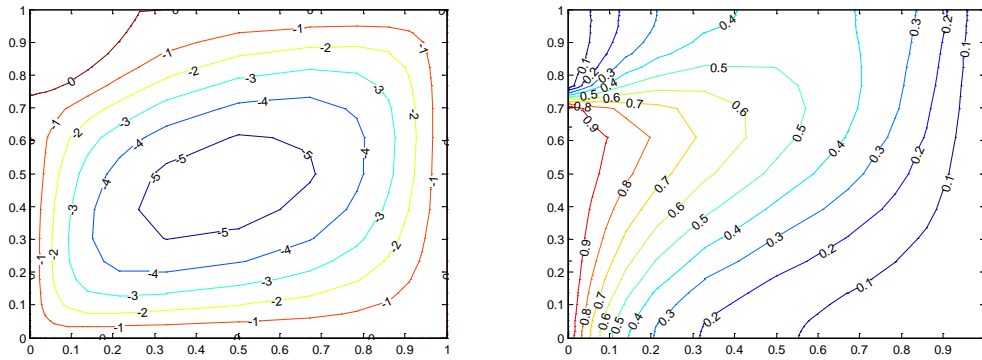
**Figure-6:** Contour plots for linearly heated vertical walls  $\theta(0, Y) = \theta(1, Y) = 1 - Y$  with  $Pr = 0.7$  and  $Ra = 10^4$ . Clockwise and anti-clockwise flows are shown via negative and positive signs of stream functions (Left) and Isotherms (Right) respectively.



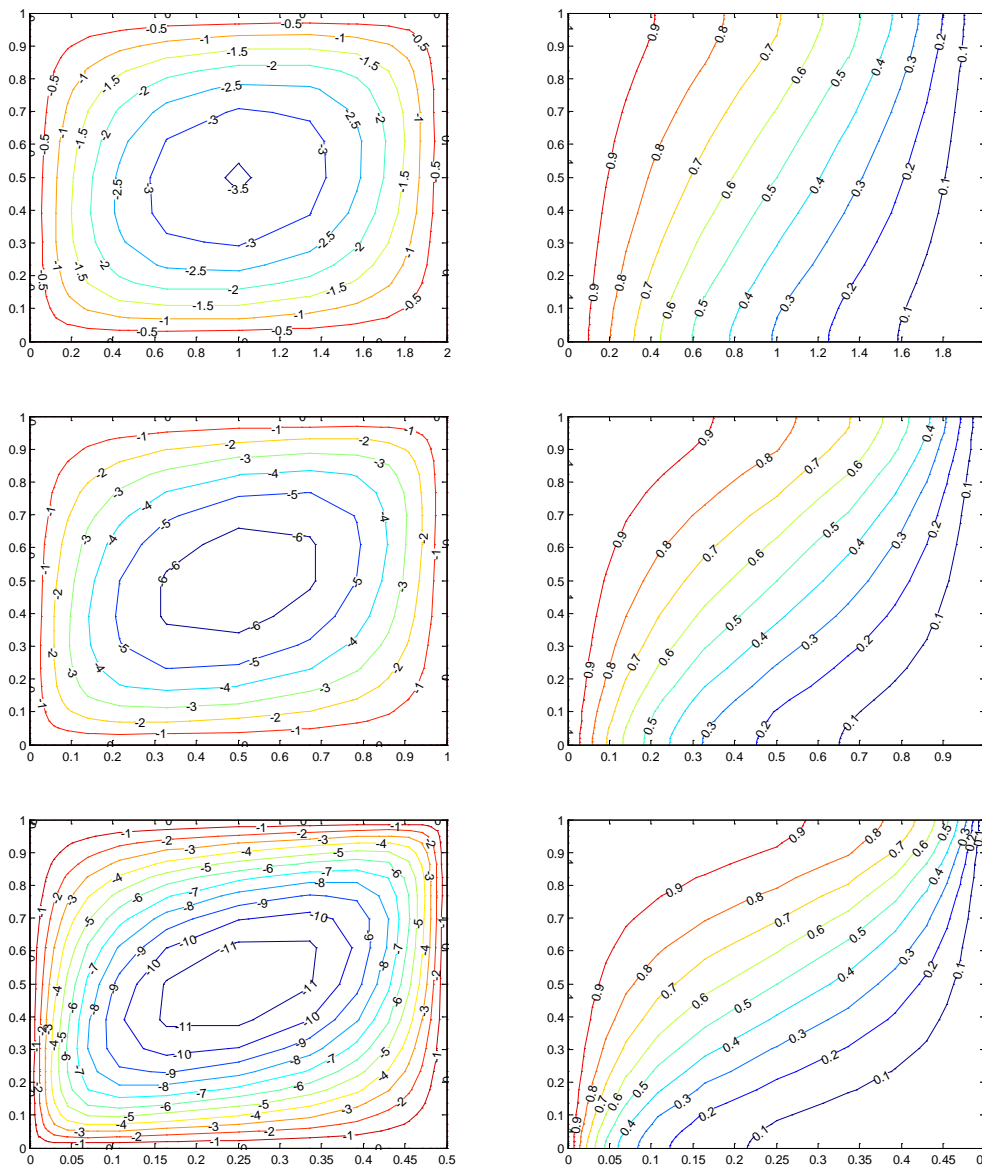


**Figure-7:** Contour plots for linearly heated vertical walls,  $\theta(0, Y) = \theta(1, Y) = 1 - Y$  with  $Pr = 0.7$  and  $Ra = 10^4$ . Clockwise and anti-clockwise flows are shown via negative and positive signs of stream functions (Left) and Isotherms (Right) respectively.

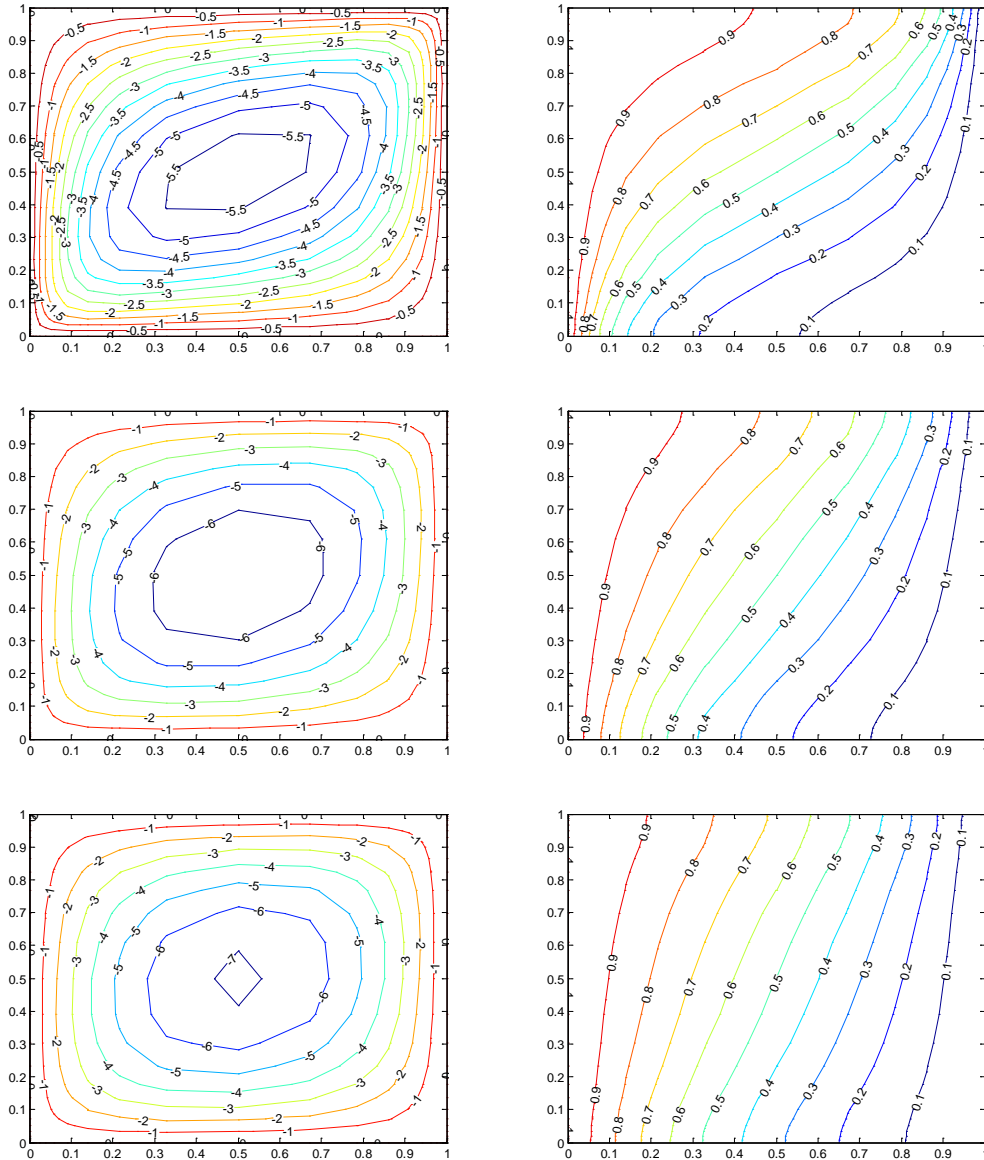




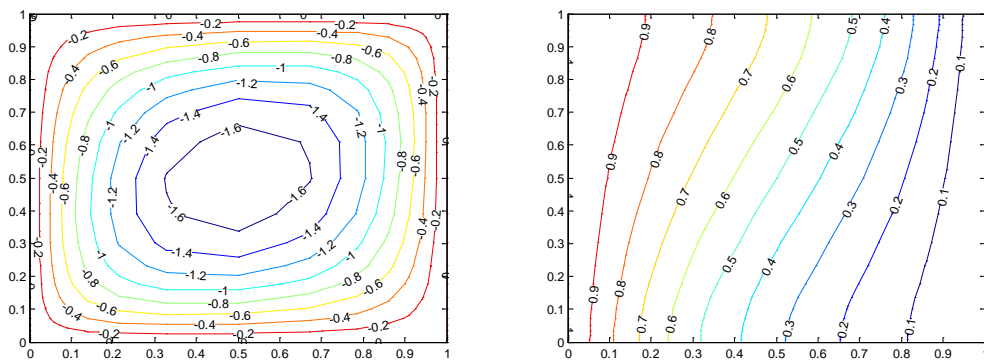
**Figure-8:** Contour plots for linearly heated vertical walls,  $\theta(0, Y) = \theta(1, Y) = 1 - Y$  with  $Pr = 0.7$  and  $Ra = 10^5$ . Clockwise and anti-clockwise flows are shown via negative and positive signs of stream functions (Left) and Isotherms (Right) respectively.

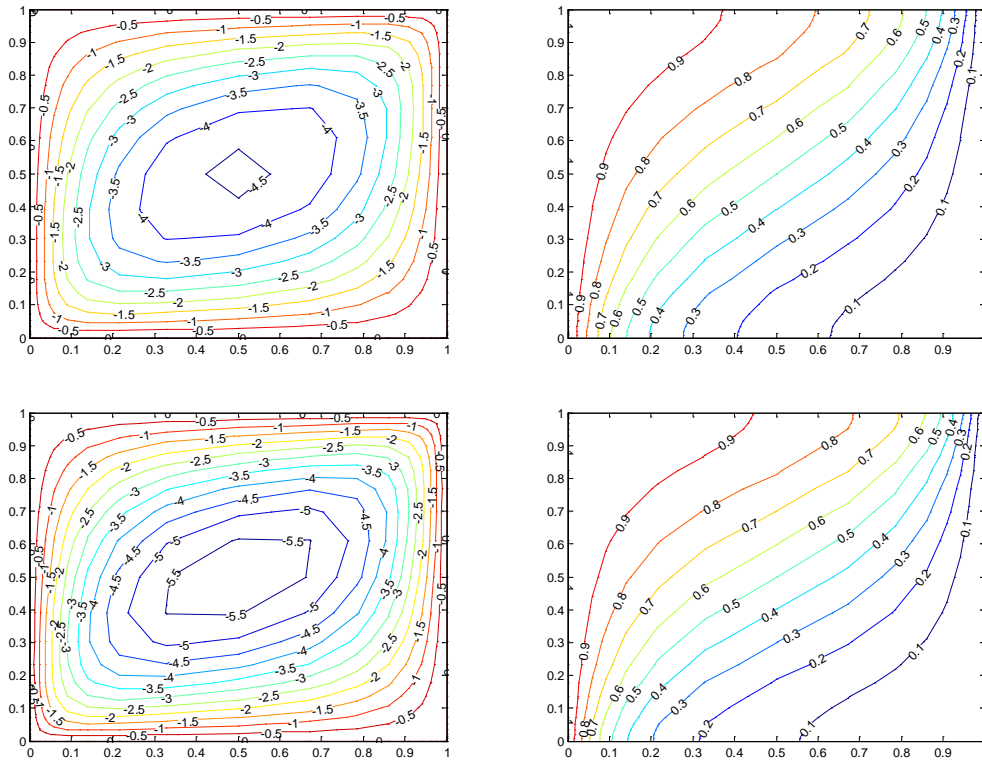


**Figure-9:** Contour plots for linearly heated vertical walls  $\theta(0, Y) = \theta(1, Y) = 1 - Y$  with  $Pr = 10$  and  $Ra = 10^5$ . Clockwise and anti-clockwise flows are shown via negative and positive signs of stream functions (Left) and Isotherms (Right) respectively.

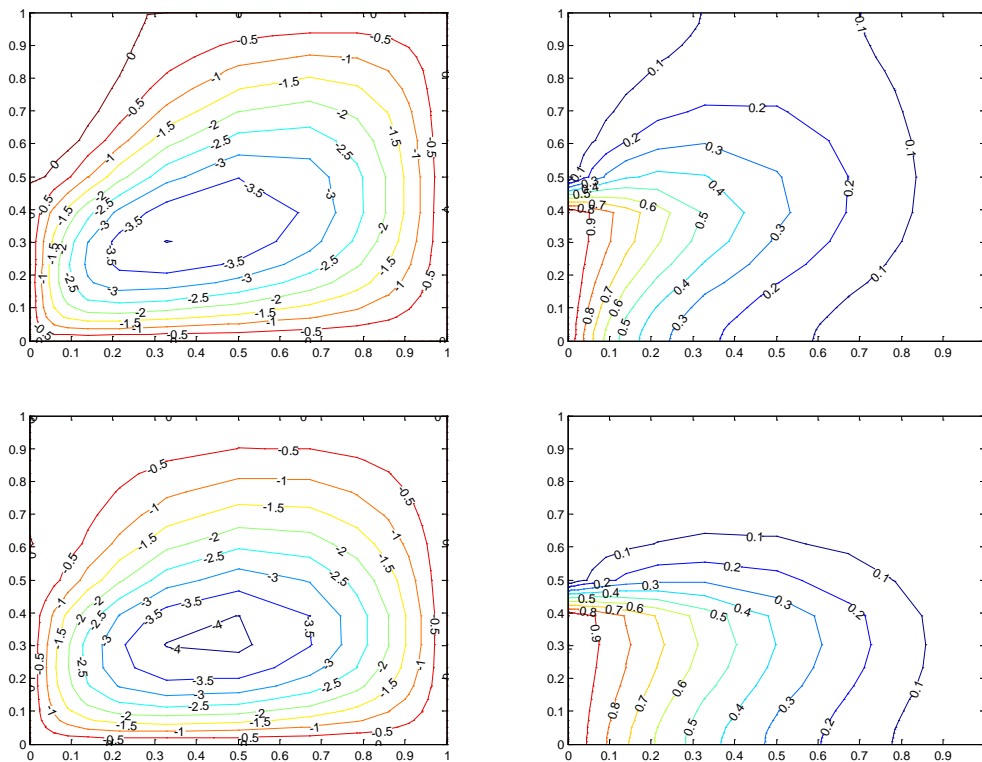


**Figure-10:** Contour plots for linearly heated vertical walls,  $\theta(0, Y) = 1 - Y$ , and cooled vertical wall  $\theta(1, Y) = 0$  with  $Pr = 0.7$  and  $Ra = 10^3$ . Clockwise and anti-clockwise flows are shown via negative and positive signs of stream functions (Left) and Isotherms (Right) respectively.





**Figure-11:** Contour plots for linearly heated vertical walls,  $\theta(0, Y) = 1 - Y$  and cooled vertical wall  $\theta(1, Y) = 0$  with  $Pr = 0.7$  and  $Ra = 10^4$ . Clockwise and anti-clockwise flows are shown via negative and positive signs of stream functions (Left) and Isotherms (Right) respectively.



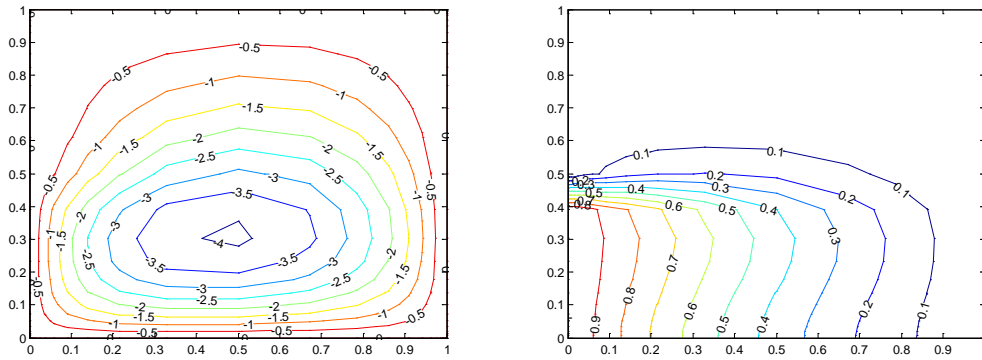


**Figure-12:** Contour plots for linearly heated vertical walls  $\theta(0, Y) = 1-Y$  and cooled vertical wall  $\theta(1, Y) = 0$  with  $Pr = 10$  and  $Ra = 10^5$ . Clockwise and anti-clockwise flows are shown via negative and positive signs of stream functions (Left) and Isotherms (Right) respectively.

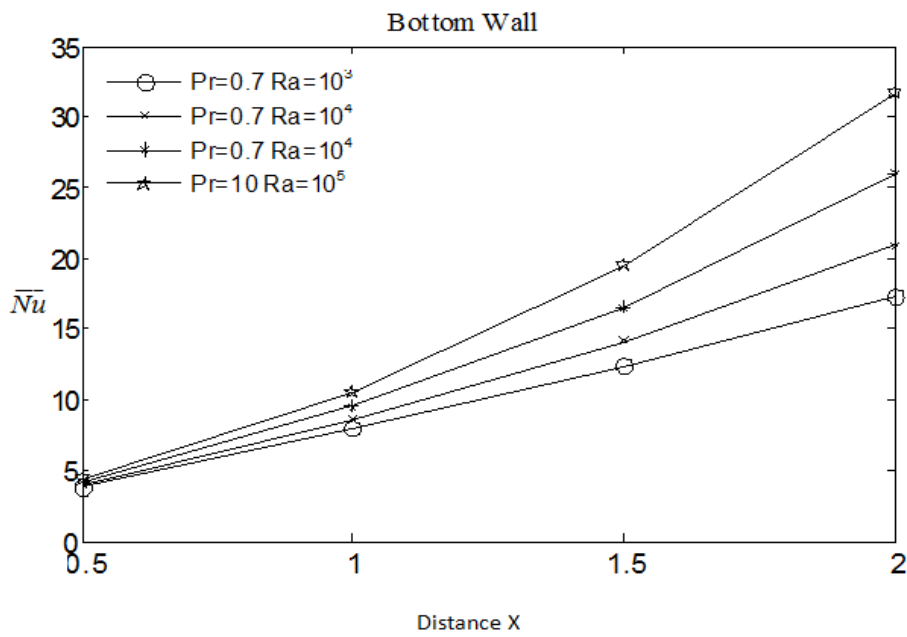


**Figure-13:**  $\bar{Nu}$  Variations with distance at bottom wall for different values of Ra

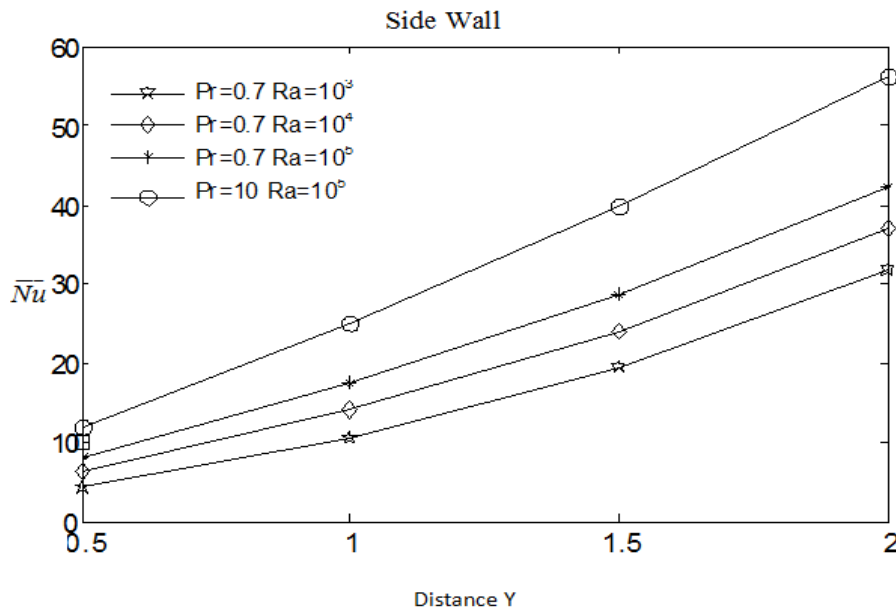


**Figure-14:**  $\bar{Nu}$  Variations with distance at side wall for linearly heated side wall for different values of Ra

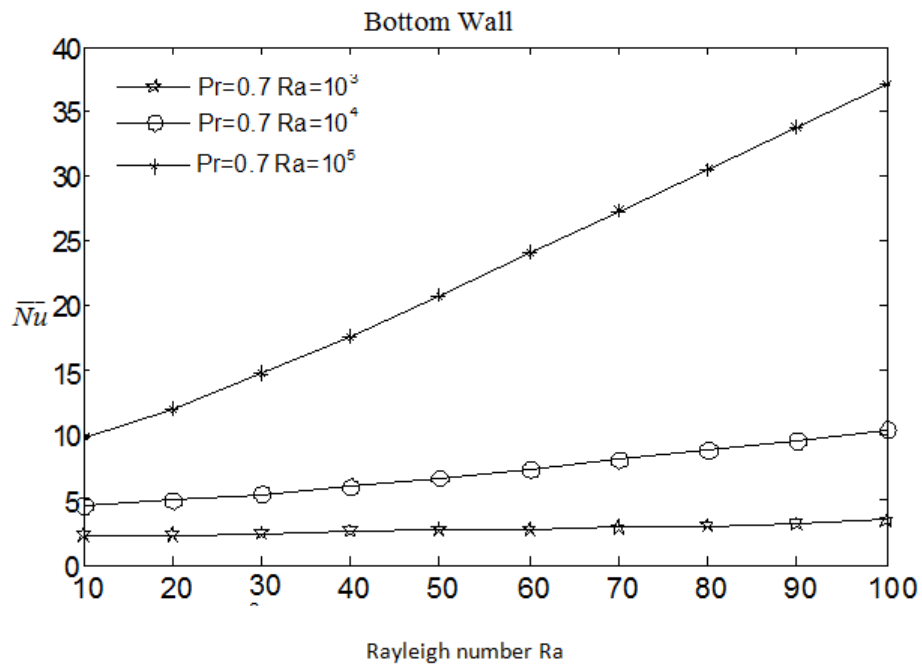


**Figure-15:**  $\overline{Nu}$  Variations with Rayleigh number for linearly heated side walls

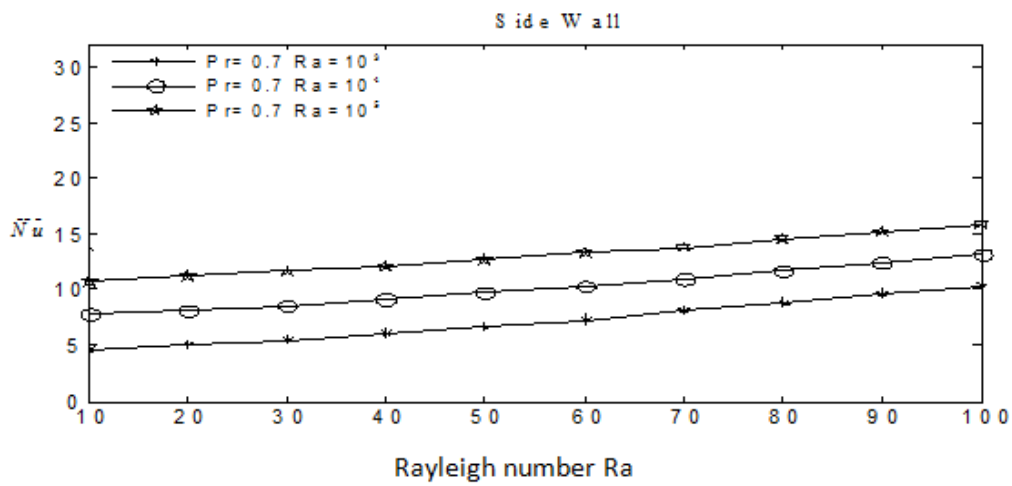


**Figure-16:**  $\overline{Nu}$  Variations with Rayleigh number for linearly heated side walls

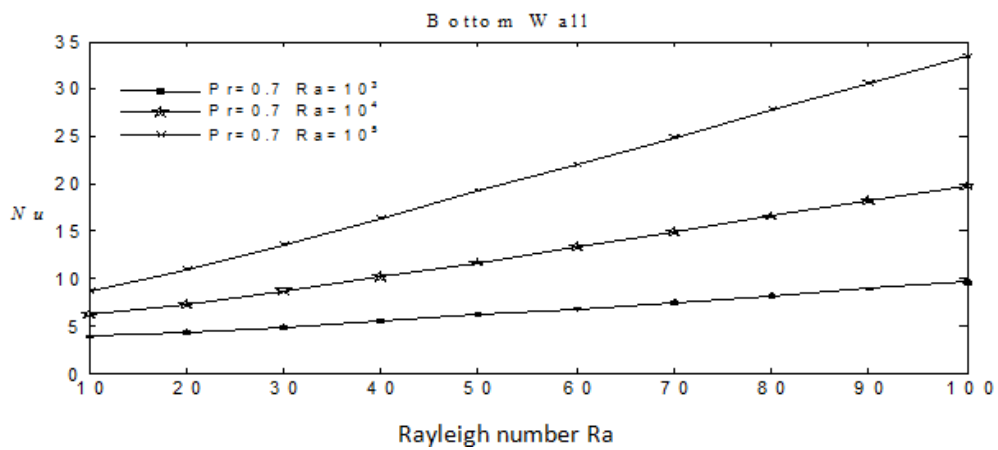


**Figure-17:**  $\overline{Nu}$  Variations with Rayleigh number for linearly heated left wall



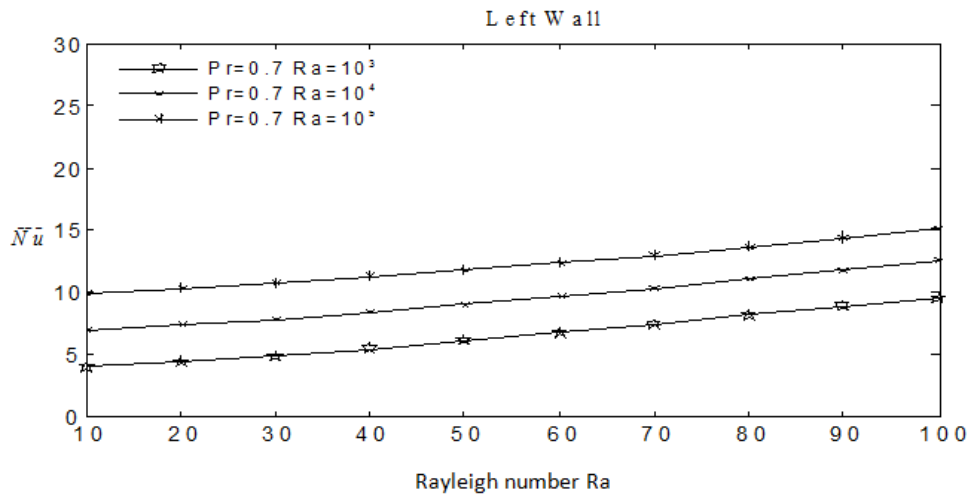


**Figure-18:**  $\overline{Nu}$  Variations with Rayleigh number for linearly heated right wall

the side wall and break into two symmetric contour lines (Fig.5) The presence of significant convection is also exhibited in Fig. 6 at  $Ra = 10^4$  where temperature contour for  $\theta = 0.6$  starts getting deformed and pushed towards the top plate. In addition, it may be noted that the secondary circulations appear at the bottom corners for  $Ra = 10^4$  due to convection as the lower half of the vertical walls are hot and the hot fluids move towards the center of the cavity. Consequently at  $Ra = 10^4$  the stronger secondary circulations enhance the mixing process which result in the rejoining of temperature contour  $\theta = 0.6$  (Fig. 7). Further at  $Ra = 10^5$  the primary circulation pushed towards the upper part of the cavity and due to enhanced convection from the linear hot vertical wall, the isotherm lines with greater values  $\theta > 0.5$  covers almost 70% of the cavity (Fig. 8). It is interesting to observe that due to two pairs of symmetric circulations, ‘hot’ and ‘cold’ fluid regimes appear distinctly across the temperature contour  $\theta = 0.6$ . In contrast at  $Ra = 10^5$  for  $Pr = 10$  the strength of secondary circulations appearing at corners of bottom wall is less as compared for  $Pr = 0.7$  case due to the viscous force dominating the buoyancy force for  $Pr = 10$  (Fig. 9). As the strength of the primary circulation increases for  $Pr = 10$  case, the isotherm lines with temperature contours  $\theta > 0.5$  covers approximately 90% of cavity. The significant effect of convective heat transfer will be illustrated later via average Nusslet number vs Rayleigh number plot. Figs. 10 –12 illustrate the stream function and isotherm contours for various values of  $Ra = 10^3-10^5$  and  $Pr = 0.7-10$  with uniformly heated bottom wall, cooled right wall and the left wall is linearly heated. As expected, due to linearly heated left wall, fluids rise up along the side of left wall and flow down along the cooled right wall forming a roll with clockwise rotation inside the cavity. As  $Ra$  increase from  $10^3$  to  $10^5$ , the value of stream function increases i.e., the flow rate increases. At the left corner of the top wall, secondary circulation formed due to convection and the hot fluids move towards the left corner of the cavity. Fig. 10 shows that the isotherm lines change its value smoothly from hot vertical wall to cold vertical wall for  $Ra=10^3$ . At  $Ra = 10^4$  the circulations are stronger and consequently the temperature contour with  $\theta = 0.5$  pushed towards the right corner of top wall (Fig. 11). At  $Ra = 10^5$  in Fig. 12 due to enhanced convection from the hot left wall to the cold right wall, the isotherm lines with greater values  $\theta > 0.5$  covers around 50% of the cavity for  $Pr = 0.7$  and  $Pr = 10$ . In addition for  $Pr = 10$ , the strength of secondary circulation increases. Fig. 13 and Fig. 14 display the effects of  $Ra$  and  $Pr$  on the local Nusselt numbers at the bottom and side walls ( $Nu_b$ ,  $Nu_s$ ) for linearly heated side walls. At the edges of the bottom wall the heat transfer rate  $Nu_b$  is 1 due to the linearly heated side walls (Fig. 13). For  $Ra = 10^4$ , the heat transfer rate is minimum value at the center of the bottom wall due to the higher values of stream function (i.e., flow rate) with two symmetric circulations about the vertical symmetric line at the center of the bottom wall. Heat transfer rate prevails at  $Ra = 10^5$  and  $Pr = 10$ . In contrast for  $Ra = 10^5$  and  $Pr = 0.7$  the heat transfer rate is maximum at center of the bottom wall due to the presence of strong secondary circulations leading to a high temperature gradient at the center of the bottom wall. In Fig.14 the heat transfer rate at the bottom-edge of side wall is zero due to uniformly heated bottom wall and the heat transfer rate is maximum at the top-edge of side wall due to insulated top wall. For  $Ra = 10^3$  and  $Pr = 0.7$ , due to weak circulations the heat transfer rate is almost zero upto  $Y = 0.7$  and  $Nu_s = 3$  at  $Y = 1$  whereas at  $Ra = 10^4$ , the heat transfer rate  $Nu_s = 4$  at  $Y = 1$  due to stronger circulations. For  $Ra = 10^5$ , due to the presence of a pair of symmetric secondary circulated cells with clockwise and anti-clockwise rotations, the heat transfer rate is oscillatory in nature in the lower half of the side walls and the increasing trend of heat transfer rate is observed in the upper half of the side walls with  $Nu_s = 6$  and  $Nu_s = 8$  at  $Y = 1$  corresponding to  $Pr = 0.7$  and  $Pr = 10$  respectively. The overall effects upon the heat transfer rates are displayed for linearly heated side walls in Fig. 15 and Fig.16, where the distributions of the average Nusselt number of bottom wall and side walls respectively are plotted vs the Rayleigh number. It is observed that the average Nusselt number is almost constant up to  $Ra = 10^4$  due to dominant heat conduction mode and smoothly increases as Rayleigh number increases further. It is interesting to note that the smoothness breaks at  $Ra = 10^4$  and  $Pr = 0.7$  for both bottom

and side walls as the oppositely rotated secondary cells becomes prominent. The smoothly increasing trend of average Nusselt numbers is observed for  $Pr = 10$  due to insignificant secondary cells. Fig. 17 and Fig. 18 display the effects of  $Ra$  and  $Pr$  on local Nusselt numbers at the bottom and side walls ( $Nu_b$ ,  $Nu_s$ ) for linearly heated left wall and cooled right wall. The heat transfer rate  $Nu_b$  is 0 at the left-edge of the bottom wall due to the linearly heated left wall and it is maximum at the right-edge of the bottom wall due to the cooled right wall (Fig. 17). As  $Ra$  increases from  $10^3$  to  $10^5$ , the heat transfer rate increases from the left edge to the right-edge of the bottom wall. In Fig. 18, the heat transfer rate at the bottom edge of the left wall is zero due to the uniformly heated bottom wall and linearly heated left wall and its magnitude increases from the bottom edge to the top edge of the left wall. At  $Ra = 10^5$ , local Nusselt number (exhibits oscillatory behavior due to the presence of secondary circulation near the top edge of the left wall. The inset plot shows the local Nusselt number distribution for the right wall. For all values of  $Ra$  and  $Pr$  it is observed that Nusselt number is maximum at the bottom edge and decreases towards the top edge.

## REFERENCES

1. Sezai, A.A. Mohamad, Suppressing free convection from a flat plate with poor conductor ribs, *Int. J. Heat Mass Transfer* 42 (1998) 2041–2051.
2. T. Pessa, S. Piva, Laminar natural convection in a square cavity: low Prandtl numbers and large density differences, *Int. J. Heat Mass Transfer* 52 (2009).
3. T. Zitzmann, M.P. Cook, P. Pfrommer, S. Rees, L. Marjanovic, Simulation of steady state natural convection using CFD, in: *Proceeding of Building Simulation, Montreal, Canada, 2005*, pp. 1–8.
4. V.A.F. Costa, Thermodynamic of natural convection in enclosures with viscous dissipation, *Int. J. Heat Mass Transfer* 48 (2005) 2333–2341.
5. G.V. Davis, Natural convection of air in a square cavity: a bench mark numerical solution, *Int. J. Numer. Methods Fluids* 3 (2005) 249–264.
6. B. Abourida, M. Hasnaoui, S. Douamma, Natural convection in a square cavity with vertical boundaries submitted to periodic temperatures, *Rev. Gen.*
7. Therm. B.S. Yilbas, S.Z. Shuja, S.A. Gradebo, H.I. Al-Hamayel, K. Boran, Natural convection and entropy generation in a square cavity, *Int. J. Energy Res.*
8. G. Barakos, E. Mitsoulis, D. Assimacopoulos, Natural convection flow in a square cavity revisited: laminar and turbulent models with walls functions, *Int. J. Numer. Methods Fluids* 18 (2005) 695–719.
9. B.A.V. Bennett, J. Hsueh, Natural convection in a cubic cavity: implicit numerical solution of two benchmark problems, *Numer. Heat Transfer A Appl.*
10. R.S. Kaluri, T. Basak, S. Roy, Bejan's heatlines and numerical visualization of heat flow and thermal mixing in various differentially heated porous square cavities, *Numer. Heat Transfer A Appl.* 55 (2009) 487–516.
11. Q.H. Deng, J.J. Chang, Natural convection in a rectangular enclosure with sinusoidal temperature distributions on both side walls, *Numer. Heat Transfer A Appl.* 54 (2008) 507–524.
12. T. Michalek, High Rayleigh number natural convection in a cubic enclosure, in: *Proceeding of Eurotherm Seminar of Numerical Heat Transfer, Gliwice- Cracow, Poland, 2005*, pp. 1–11.
13. E. Bilgen, H. Oztop, Natural convection heat transfer in partially open inclined square cavities, *Int. J. Heat Mass Transfer* 48 (2005) 1470–1479.
14. F. Kuznik, J. Vareilles, G. Rusaouen, G. Krauss, A double-population lattice Boltzmann method with non-uniform mesh for the simulation of natural convection in a square cavity, *Int. J. Heat Fluid Flow* 28 (2007) 862–870.
15. Mezrhab, M. Jami, C. Abid, M. Bouzidi, P. Lallemand, Lattice-Boltzmann modelling of natural convection in an inclined square enclosure with partitions attached to its cold wall, *Int. J. Heat Fluid Flow* 27 (2006) 456–465.
16. Bahlaoui, A. Raji, R. El Ayachi, M. Hasnaoui, M. Lamsaadi, M. Naïmi, Coupled natural convection and radiation in a horizontal rectangular enclosure discretely heated from below, *Numer. Heat Transfer A Appl.* 52 (2007) 1027–1042.
17. R. El Ayachi, A. Raji, M. Hasnaoui, A. Bahlaoui, Combined effect of radiation and natural convection in a square cavity differentially heated with a periodic temperature, *Numer. Heat Transfer A Appl.* 53 (2008) 1339–1356.
18. J.F. Hinojosa, C.A. Estrada, R.E. Cabanillas, G. Alvarez, Numerical study of transient and steady-state natural convection and surface thermal radiation in a horizontal square open cavity, *Numer. Heat Transfer A Appl.* 48 (2005) 179–196.
19. G.V. Kuznetsov, M.A. Sheremet, Conjugate heat transfer in an enclosure under the condition of internal mass transfer and in the presence of the local heat source, *Int. J. Heat Mass Transfer* 52 (2009) 1–8.
20. A.B. Nakhi, A.J. Chamkha, Conjugate natural convection around a finned pipe in a square enclosure with internal heat generation, *Int. J. Heat Mass Transfer.*
21. H. Oztop, E. Bilgen, Natural convection in differentially heated and partially divided square cavities with internal heat generation, *Int. J. Heat Fluid Flow.*
22. H.F. Oztop, E. Abu-Nada, Numerical study of natural convection in partially heated rectangular enclosures filled with nanofluids, *Int. J. Heat Fluid Flow.*

23. Bazylak, N. Djilali, D. Sinton, Natural convection in an enclosure with distributed heat sources, Numer. Heat Transfer A Appl. 49 (2006) 655–667.
24. É. Fontana, A. Silva, V.C. Mariani, F. Marcondes, The influence of baffles on the natural convection in trapezoidal cavities, Numer. Heat Transfer A Appl. 58 (2010) 125–145.
25. S. Sivasankaran, C.J. Ho, Buoyancy- and thermocapillary-induced convection of cold water in an open enclosure with variable fluid properties, Numer. Heat Transfer A Appl. 58 (2010) 457–474.
26. T.H. Hsu, K.Y. Hong, Natural convection of micropolar fluids in an open cavity, Numer. Heat Transfer A Appl. 50 (2006) 281–300.
27. A. Andreozzi, O. Manca, Numerical investigation on the steady state natural convection in a horizontal open-ended cavity with a heated upper wall, Numer. Heat Transfer A Appl. 57 (2010) 453–472.
28. V.C. Mariani, A. Silva, Natural convection: analysis of partially open enclosures with an internal heated source, Numer. Heat Transfer A Appl. 52 (2007) 595–619.
29. V.C. Mariani, L.S. Coelho, Partially open enclosures containing an internal local heat source, Braz. J. Chem. Eng. 24 (2007) 375–388.
30. P. Kandaswamy, J. Lee, A. Hakeem, Natural convection in a square cavity in the presence of heated plate, Nonlinear Anal. Model. Control 12 (2007) 203–212.
31. M. Hortmann, M. Peric, G. Scheuerer, Finite volume multigrid prediction of laminar natural convection: benchmark solutions, Int. J. Numer. Methods Fluids 11 (1990) 189–207.
32. J.L. Xia, Z.W. Zhou, Natural convection in an externally heated partially open cavity with a heated protrusion, FED-vol. 143/HTD, Measurement and Modeling of Environmental Flows – ASME, vol. 232, 1992, pp. 201–208.

**Source of support: Nil, Conflict of interest: None Declared.**

***[Copy right © 2018. This is an Open Access article distributed under the terms of the International Journal of Mathematical Archive (IJMA), which permits unrestricted use, distribution, and reproduction in any medium, provided the original work is properly cited.]***